JOURNAL OF MATERIALS SCIENCE **38** (2003) 3143–3153

Morphological features of the crystalline or quasicrystalline silicides observed in the quaternary Al-Fe-Mo-Si alloys

M. C. S. DE MACÊDO
Departamento de Engenharia Mecânica (DEM), Universidade Federal do Espírito Santo (UFES), Av. Fernando Ferrari s/no—Campus de Goiabeiras, CEP: 29060-970, Vitória-ES, Brasil
E-mail: mcamargo@npd.ufes.br

G. MICHOT
Laboratoire de Physique des Matériaux, UMR CNRS 7556, Ecole des Mines de Nancy, Parc de Saurupt, 54042 Nancy Cedex, France

Rapidly solidified Al-Fe-Mo-Si powders were produced by centrifugal atomization and then consolidated by hot extrusion. Five compositions were chosen in order to obtain a theoretical constant volume fraction of (silicide + $Al_{12}Mo$) of 20%, with different relative fractions of [silicide]/[α-matrix] and different ratios of [Fe]/[Mo] within the silicide. This paper presents the microstructures observed in both as-atomized and consolidated states. The only phase detected by X-Ray Diffraction, the non equilibrium ternary $Al_{12\text{-}13}(Fe,Mo)_3Si$, exhibits different sizes and morphologies and is inhomogeneously distributed within the matrix. Accurate electron microscopy observations indicate that this silicide may grow from a quasicrystalline precursor. Grains within the polycrystalline silicide often exhibit orientation relationships (micro twinning) giving rise to quasicrystalline-like patterns.

1. Introduction

Due to the problem of strength loss resulting from overaging at service temperature, heat treatable aluminium alloys are not suitable for high temperature applications. This can be avoided through hardening by thermally stable intermetallic compounds or oxides and/or carbides. The aeronautical industry needs for lightweight creep resistant alloys impose the choice of aluminum based alloys. By addition of transition elements, and/or, rare earth metals, to aluminum whose solubility and diffusivity are very low, intermetallic compounds that remain stable up to 300 to 400°C can be easily precipitated. Since the processing of such alloys through ingot metallurgy will promote precipitation of embrittling coarse particles, rapid solidification from the melt is required. Among possible candidates, those based on the Al-Cr and Al-Fe systems have led to industrial development: extrusions, sheets or forgings of Al-Cr-Zr, Al-Fe-Ce alloys (8019) and Al-Fe-V-Si alloys (8009) are already available and exhibit improved properties at high temperature as compared to conventional 2024-T3 or 7175-T7 alloys.

Processing the Al-Fe-Si alloy family through rapid solidification route results in the precipitation of very fine, round shaped Al-Fe-Si phase, hence, a high level of mechanical properties is achieved. Introduction of a fourth element such as vanadium stabilizes the BCC $Al_{12\text{-}13}(Fe,V)_3Si$ phase improving the Ostwald ripening resistance and hence delaying the formation of the stable Al_8Fe_2Si (hexagonal) and Al_3Fe (monoclinic) phases. This alloy exhibits a coarsening rate that is two to three times lower than the current alloys [1]. Such a stabilization is attributed to modification of the matrix/silicide interface's energy through changes in lattice mismatch due to substitution of vanadium on the iron sites [2, 3].

The main limitations in the development of this alloy are the formation of the Al_3Fe equilibrium phase above 727°C [4, 5] and the existence of a ductility drop due to dynamical strain aging. In classical aluminum alloys containing fast diffusers, this latter phenomenon takes place at room temperature. For high temperature aluminum alloys, the lower diffusivity of the alloying elements makes this phenomenon appear at a higher temperature range [6, 7], which is likely to be chosen for further material forming.

For this study Mo was chosen rather than V in order to obtain a finer precipitation [8], postpone the formation of the embrittling Al_3Fe phase [9], and take advantage of a possible hardening by $Al_{12}Mo$. Finally, the lower diffusivity of Mo compared to V could shift the dynamic strain aging effect towards still higher temperatures. To check respectively the influence of the silicide and the $Al_{12}Mo$ phases, and of the ratio [Fe]/[Mo] in

TABLE I Chemical compositions, theoretical volume fraction (%) and atomic ratio [Fe]/[Mo] in the silicide, alloys nomenclature. The theoretical volume fraction, [silicide] + [$Al_{12}Mo$], is 20%

Nominal compositions	Silicide (%)	[Fe]/[Mo]	Nomenclature
Al-3.68 Fe-0.25 Mo-1.31 Si	20	15/1	2015/1
Al-3.57 Fe-0.36 Mo-1.31 Si	20	10/1	2010/1
Al-3.27 Fe-0.66 Mo-1.31 Si	20	5/1	205/1
Al-2.50 Fe-0.80 Mo-1.00 Si	16	5/1	165/1
Al-1.99 Fe-0.99 Mo-0.85 Si	12	5/1	125/1

the silicide, several alloys compositions were studied (please refer in Table I).

2. Experimental procedure

The alloys were prepared at 1250°C under argon by induction melting pure aluminum, Al-Fe and Al-Si master alloys, and molybdenum chips under a boron nitride film protection. Then there was homogenization for 45 min and finally, chill casting in a graphite mould. The obtained ingot was re-melted and homogenized for 15 min. Centrifugal pulverization was used as the processing route instead of the planar flow technique industrially developed for manufacturing the 8009 alloy. This procedure was carried out in a device described by Ziani and Michot [10]: when the melted alloy was overheated up to ∼150°C above the liquidus temperature, the melt was streamed through the crucible nozzle onto a spinning disk to be divided on its periphery into small elongated droplets which evolved to spherical ones during solidification. The metal flow rate was generally between 1 and 5 g/s. Half of the powder mass obtained is composed of particles with a diameter smaller than 80 μm. The powder batch is then divided into different size fractions. The 50 to 100 μm fraction considered in this study is canned and degassed at 350°C for 3 h. The can is sealed and extruded at 400°C through a conical die (extrusion ratio 25:1) under a ram speed of 0.76 mm/s. Phase determination is mainly achieved through X-ray diffraction (XRD) using filtered Co K_α radiation. The microstructures are characterized by electron microscopy (SEM and TEM). Table II presents the chemical analysis results for the different alloys. The obtained compositions (oc) are close to the aimed compositions (ac).

3. Powder characterization

3.1. Phase identification

Neither the Al_3Fe nor the $Al_{12}Mo$ stable phases are detected in the powder by XRD. Except for the α-Al matrix diffraction peaks, the other peaks are very similar to those reported by Vadusevan and Fraser [9] for the Al-Fe-Mo-Si silicide. A decrease in the lattice parameter of the silicide phase with the [Fe]/[Mo] ratio and an opposite variation of the matrix parameter were noticed. It can be deduced that:

– substitution of Mo on the Fe sites has the same effect as Cr or V [8], thus the matrix/silicide interface energy could be monitored through substitution of Mo to Fe in order to decrease Ostwald ripening,

– the least Mo there is in the silicide, the lower will be the Mo supersaturation in the matrix (the lattice parameter of the α-Al decreases with the Mo content [11, 12]).

TABLE II Chemical analysis results (ac = aimed composition and oc = obtained composition)

	2015/1		2010/1		205/1		165/1		125/1	
Element	a.c.	o.c.	a.c.	o.c.	a.c.	o.c.	a.c.	o.c.	a.c.	o.c.
Fe	3.68	3.21	3.57	3.25	3.27	3.09	2.50	2.33	1.99	1.79
Mo	0.25	0.25	0.36	0.32	0.66	0.59	0.80	0.54	0.99	0.74
Si	1.31	1.07	1.31	1.3	1.31	1.26	1.00	0.85	0.85	0.70

3.2. Microstructures

3.2.1. Particles' surface

The powder particles are nearly spherical. A large number of different microstructures can be observed on surfaces of as-solidified particles which can be either precipitation free and cell type (Fig. 1a), or smooth (Fig. 1b) or partially free (Fig. 1c), or showing cells originating from precipitates (Fig. 1d).

During the atomization process, as soon as solidification starts, the hypothesis of an externally driven radial heat flow stops to hold true [13, 14]. A solidification mechanism in which the solidification front moves from the exterior outside towards the bulk of the particle cannot account for the observed microstructures. In other words the freezing conditions and the shape of the solidification front will depend on prior undercooling and local heat flow. This is very much influenced by nucleation events and thus, local latent heat release. Large undercooling prior to solidification is expected from the atomization technique because the small size of the "ingot" limits the number of potential nuclei and because solidification takes place without contact with a mould wall. Could such conditions lead to the predendritic growth described many years ago [15] and subsequently observed in some rapidly solidified alloys? Such growth requires an undercooling important enough for the liquid to transform itself into a solid without any change in the composition, i.e., through a diffusionless process. Such a mechanism seems to take place in the particle shown in Fig. 1c. The observation suggests that undercooling of the particle is large enough for nucleation to take place (somewhere on the smooth part of the particle) and for the solidification front to be quickly driven up to the point of completion of recalescence (on an outer part of the smooth zone). Then, solidification will take place at a temperature close to that of equilibrium, with a smaller rate imposed by the thermal exchange with helium gas. This slowing down of the front mobility enhances the diffusion in the liquid and results in an increase in size of the silicides with distance to the nucleation point. The composition of the smooth part must be very close to that of the alloy. On the contrary, it appears that the brighter inner part of the radial features observed in Fig. 1d contains a much higher proportion of heavy elements than the darker surrounding matrix. This suggests

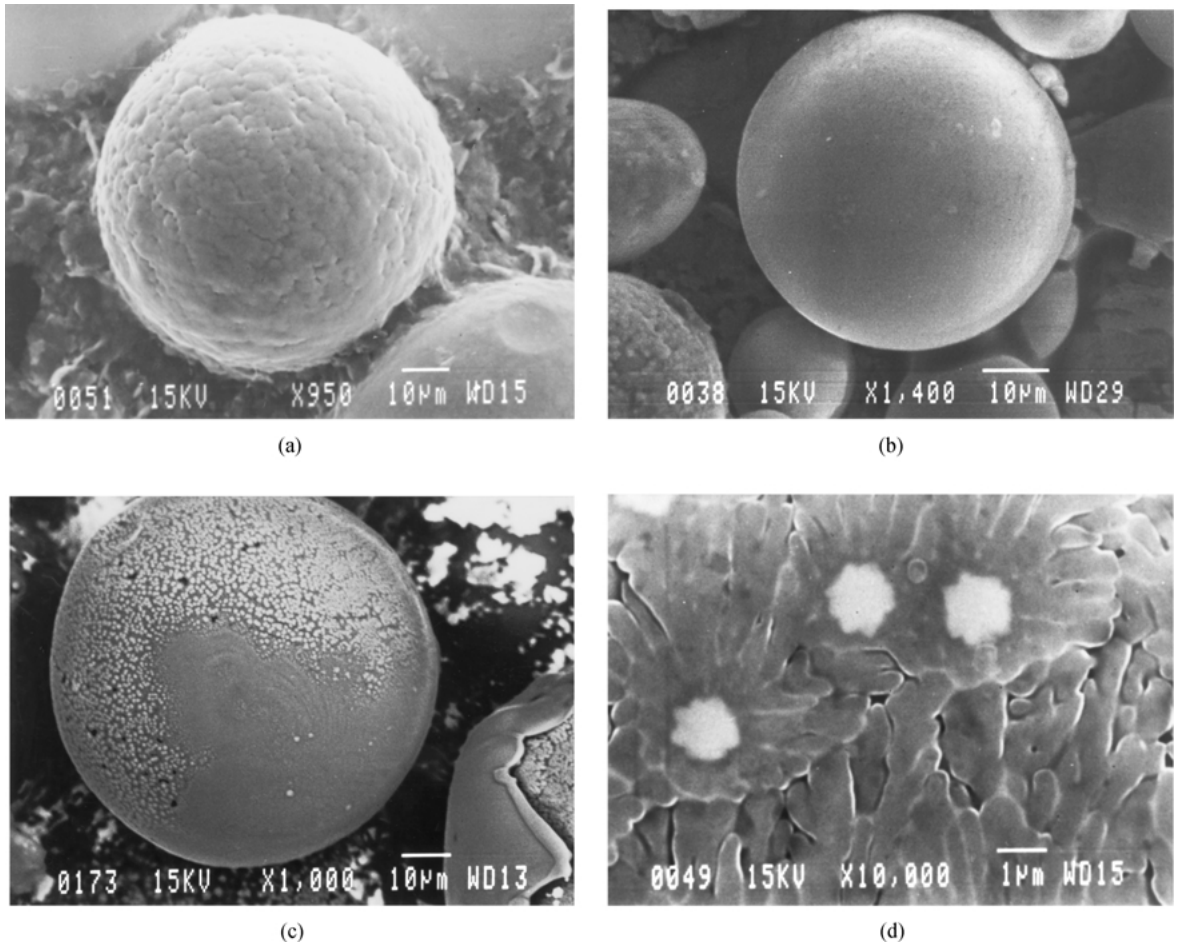

Figure 1 SEM observations: (a) cellular solidification (alloy 165/1, secondary electrons), (b) smooth particle (alloy 2010/1, secondary electrons), (c) heterogeneous microstructure of a particle surface (alloy 205/1, secondary and backscattered electrons), and (d) matrix cellular growth from the surface precipitates (alloy 165/1, secondary electrons).

that an intense surface, as well as a bulk precipitation precedes a cellular radial growth. The observation of cells (Fig. 1a) on the whole surface implies that external surface is the ultimate position of the solidification front, i.e., solidification is not controlled by the cooling atmosphere but by the undercooling which allowed nucleation in the bulk of the particle.

3.2.2. Particles cross section

Observation of the sections (Fig. 2a, b and c), confirms the non radial character of solidification. An exception can be noticed perhaps on some uniform depleted zone noticed on the outer part of the particles (Fig. 2d). Fig. 2a has to be correlated with Fig. 1c. A transition is observed between the undercooled regime (precipitate free zone) and the quasi-equilibrium regime (silicide precipitation). In the same way, Fig. 2b and c could be linked to Fig. 1d. The depleted zones are observed both when a transition from precipitate free to near equilibrium regime occurs and when the undercooling is low, in other words, in the absence of such transition (Fig. 2d).

The increase in particle's size next to the precipitate free zone means that there is a velocity decrease of the solidification front which moves from the particle's interior to the particle's exterior at temperatures close to equilibrium. As there is no coarse silicide precipitation in the precipitate free zone after heat treatment, it is probable that most part of the solute was used up during the coarse precipitation at the zone boundary, or that the outer shell was solidified before rejecting the solute, or that it was solidified in the end because the amount of solute in the remaining liquid was low and of a low melting point. In both situations, the thermal regime is controlled simultaneously by undercooling and by convection [13], but the heat flux is radial, as seen in micrographs 2a and 2c, which show the orientation of the cellular precipitation.

3.2.3. Phase morphologies

Scanning electron microscopy shows at least two different precipitate morphologies. The first one, (Fig. 3), is a type of composite phase presenting a shell of precipitates surrounding a core of a different nature ("doughnuts"), probably resulting from thinning (TEM observation) or polishing (SEM observation). This affirmation is based on the fact that the core is preferentially attacked by the Keller reagent.

The second morphology (Fig. 4) corresponds to a bulky form, almost polygonal. The cellular microstructure developed in the powder is fine and can sometimes not be resolved by SEM.

Transmission electron microscopy observations indicate microstructural variations which probably

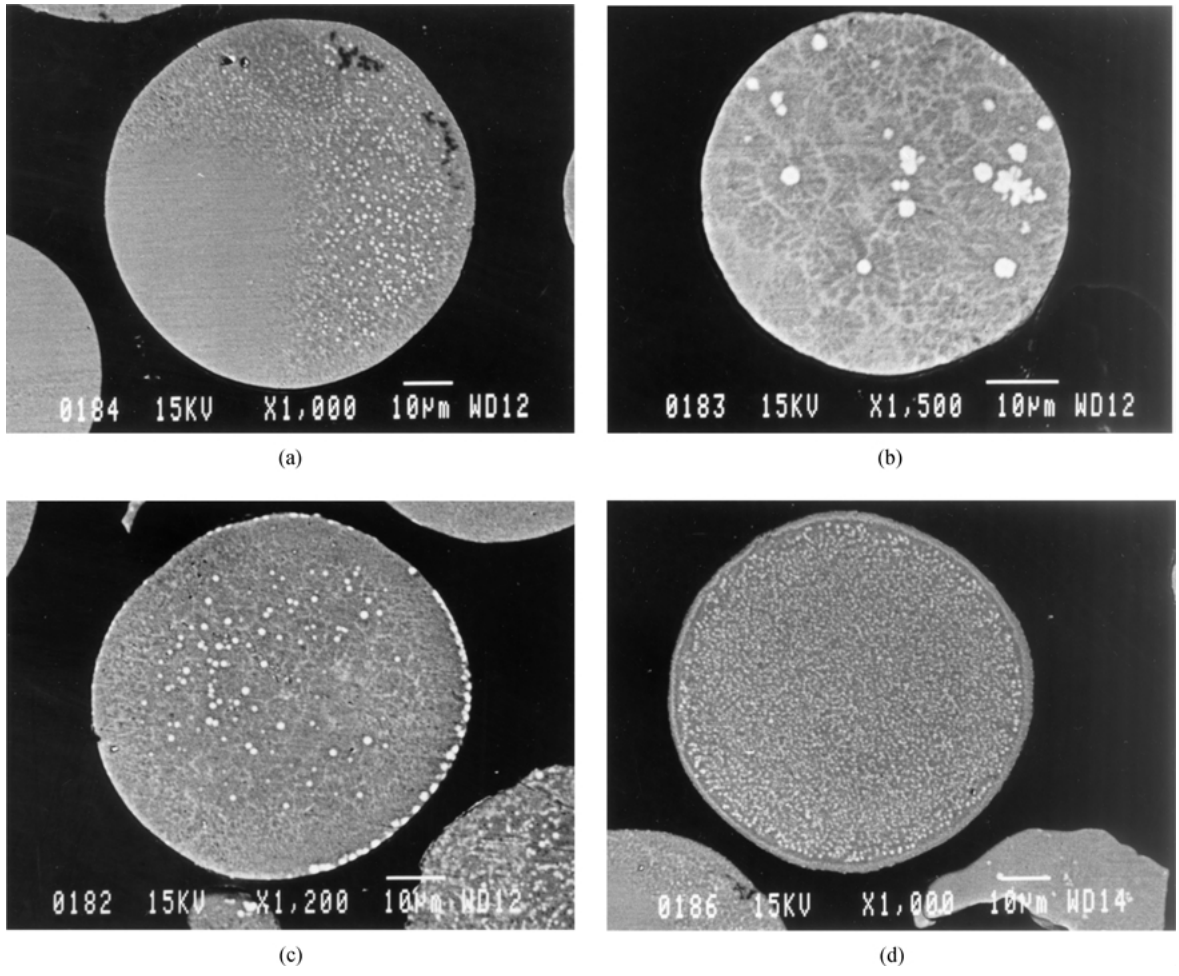

Figure 2 SEM observations of particle sections. Solidification microstructure (Keller reagent—5 s): (a) transition between a precipitate free zone and a region with second phases (alloy 2010/1, backscattered electrons), (b) matrix cellular growth from the inner precipitates (alloy 2010/1, backscattered electrons), (c) surface and inner nucleation (alloy 2010/1, backscattered electrons), and (d) outer silicide free zones (alloy 205/1, secondary and backscattered electrons).

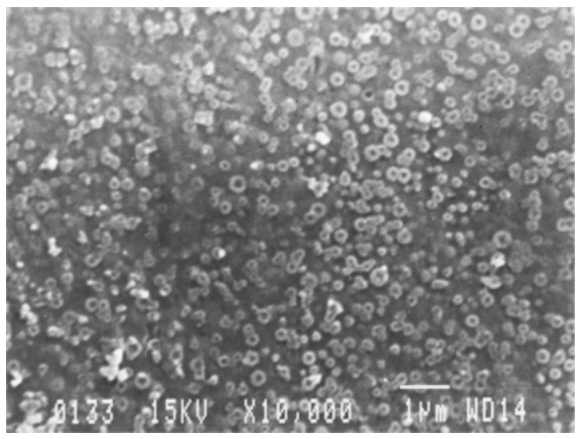

Figure 3 SEM observation of a particle section (alloy 165/1, secondary electrons, Keller reagent—5 s): composite precipitates.

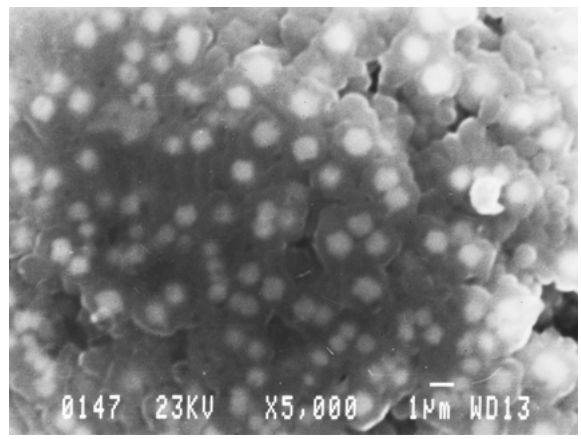

Figure 4 SEM observation of a particle surface (alloy 2015/1, secondary electrons, Keller reagent—5 s): bulky morphology, almost polygonal.

represent changes in the solidification rate (Figs 5 to 9). This leads to different sizes of microcells (from 0.1 μm in Fig. 5 to 0.6 μm in Fig. 6). At least five different microstructures could be distinguished: a more or less continuous inter-cellular precipitation of silicides (Fig. 6), distinct silicides (Fig. 7), bulky polygonal precipitates (Fig. 8), aggregates forming nodular precipitates, and composite phase precipitation (Fig. 9). The two latter types will be described in details in Section 4.2.2. Most of these microstructures were also detected in Al-Fe-V-Si alloys produced by melt spinning or atomization [8, 16–19].

The dispersoids are thought to form directly from the supersaturated liquid. Their growth interferes with the moving solid/liquid interface. According to [19], the precipitation is mainly intercellular at low solidification rate. Higher solidification rates lead to a deepening of the grooves at the cell boundary and subsequent

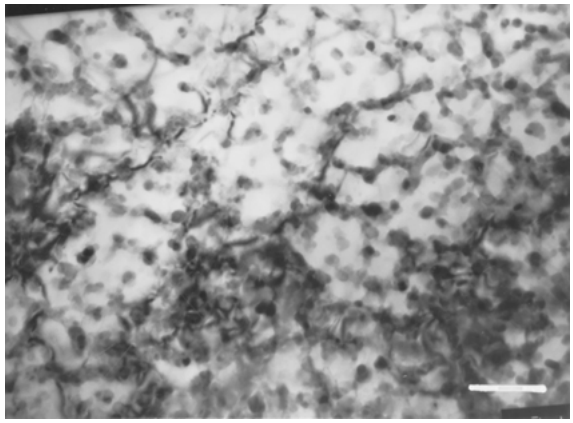

Figure 5 TEM observation of cell decomposition into distinct precipitates (marker = 0.25 μm).

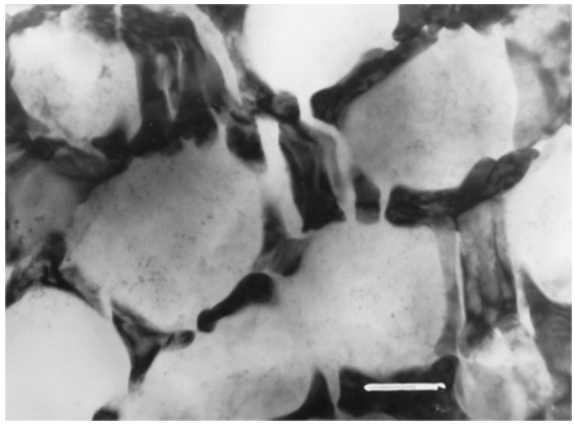

Figure 6 TEM observation of cell walls formed by semi-continuous silicides (marker = 0.3 μm).

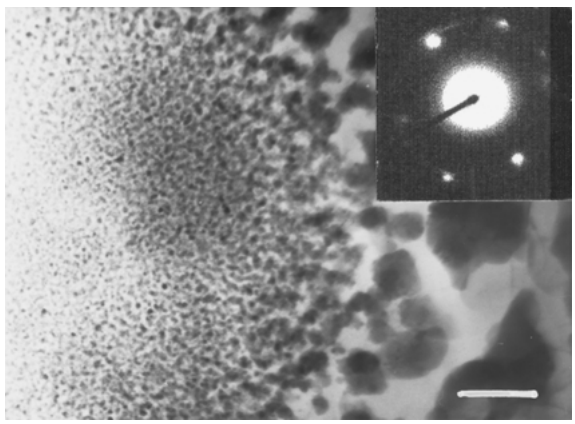

Figure 7 TEM observation of a transition zone from fine silicides to coarse cells (marker = .4 μm). The diffraction pattern presented is relative to the region of fine precipitation. (011) matrix plane. The external ring corresponds to the main diffracting plane of the silicide (611/532, see Table III).

collapse of the side walls to pinch off liquid droplets. This gives rise to a characteristic dispersoid morphology. Very similar morphologies are noticed here. Observations at higher magnification confirm that the intercellular phase is discontinuous (Fig. 7) but, because of the rounded shapes of the silicides, one can suspect some decomposition through an Ostwald ripening mechanism during recalescence [3, 16]. Different steps of this decomposition can be seen Figs 5 to 7 (all

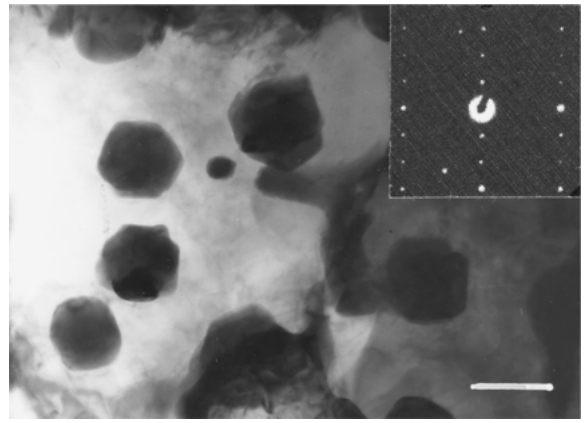

Figure 8 TEM observation of bulky silicides with polygonal form (marker = 0.4 μm). (035) cubic silicide plane.

TEM micrographs presented in this section are obtained from composition 165/1). Recalescence is also probably at the origin of the decrease in the solidification rate leading to a coarsening of the silicides shown in Fig. 7.

4. Characterization of the as-consolidated material

4.1. Phase identification

In as-consolidated alloys, only silicides were detected by X-ray diffraction (Table III). After 100 h at 480 or 550°C, the $Al_{12}Mo$ phase precipitates only in alloys with an Mo content greater than 0.7 at.% (165/1 and 125/1). In this case the precipitation occurs more easily than for the R.S powder, since the peaks related to this phase appear only after 100 h at 300°C for the 125/1 alloy [20]. The same behavior was already observed in Al-Mo binary alloys [20]. In the alloys containing only the silicide (2015/1, 2010/1 and 205/1) the $Al_{12}Mo$ phase is only detected after 100 h at 550°C (the silicide decomposes and releases Mo atoms that precipitate as $Al_{12}Mo$). This phase is stable until around 700°C.

The amount of Mo in solution in the matrix or in the silicide could be estimated by measuring the lattice parameters. Even though the calculation of absolute concentration is not necessarily accurate enough, it helps in estimating the variation. Table IV presents the results obtained for the matrix.

In the as-extruded condition, always considering experimental inaccuracy, it could be assumed that the solid solution was not surpersaturated for alloys with theoretical volume fraction of 20% of silicide (2010/1 et 205/1) because the lattice parameter is close to that of pure aluminum (4.0496 Å). During extrusion, diffusion of the iron and silicon atoms (facilitated by strong plastic deformation) is high enough to allow the precipitation of silicides around the Mo atoms: all molybdenum available is thus consumed for its formation. Alternatively, the lattice parameters of the alloys capable of $Al_{12}Mo$ phase precipitation are lower than the pure aluminum parameter. As it has been mentioned before, we can suppose that all the silicides were precipitated and that the supersaturation detected was due

TABLE III Identification of the silicide Al-Fe-Mo-Si phase in the as-consolidated alloys (n.b.: spp Al means superposition with a matrix peak)

Silicide peaks	Vasudevan *et al.* [9]		2010/1	205/1	165/1	125/1
	I/I_0	d (Å)	d (Å)	d (Å)	d (Å)	d (Å)
220	17	4.47	4.4584	4.4758	4.4612	4.4666
310	45	3.99	3.9816	4.0012	3.9916	4.0011
222	17	3.65	3.6354	3.6552	3.6422	3.6568
321	18	3.37	3.3664	3.3831	3.3748	3.3825
431/510	16	2.48	2.4697	2.4816	2.4727	2.4770
521	28	2.31	spp Al	spp Al	spp Al	spp Al
433/530	71	2.16	2.1603	2.1705	2.1641	2.1666
600	33	2.10	2.0991	2.1095	2.1024	2.1055
532/611	100	2.05	2.0432	2.0528	2.0466	2.0496
620	19	2.00	1.9902	spp Al	spp Al	spp Al
770/853/941	20	1.27	1.2733	1.2803	1.2744	1.2763
a mean (Å)	12.63 ± 0.03		12.597 ± 0.009	12.651 ± 0.013	12.617 ± 0.008	12.641 ± 0.012

TABLE IV Evolution of the matrix lattice parameter a (Å), with composition (the given uncertainty corresponds to the standard deviation in the fit of the curve a (cotgθ) plus the experimental inaccuracy which is of about 10^{-4})

Condition	2010/1	205/1	165/1	125/1
As-extruded	$4.0487 \pm 8 \times 10^{-4}$	$4.0503 \pm 6 \times 10^{-4}$	$4.0485 \pm 7 \times 10^{-4}$	$4.0478 \pm 5 \times 10^{-4}$

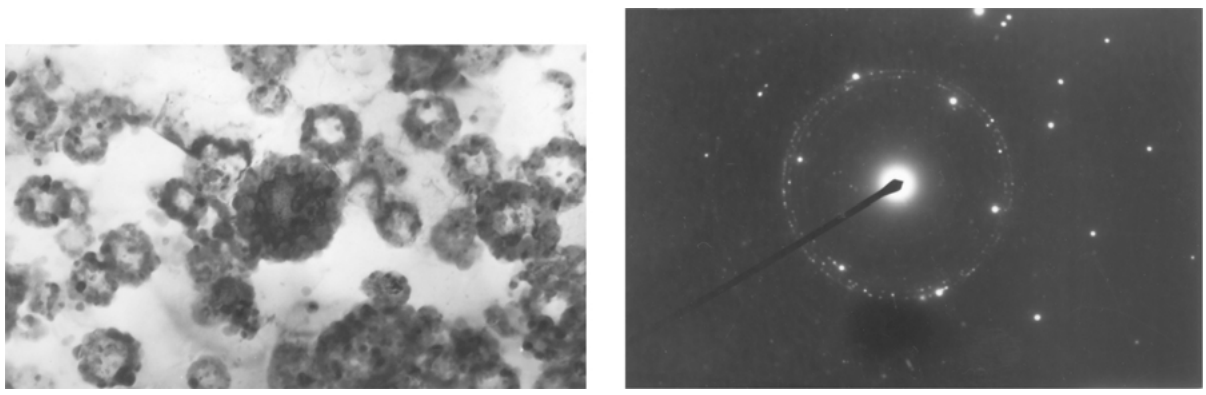

Figure 9 TEM observation of different features of the composite precipitates according to its position within the sample (marker = 0.3 μm, alloy 165/1). Diffraction pattern on the core of the central precipitate (black) corresponds to a (011) plane of aluminum.

to an excess of Mo atoms (the molybdenum did not precipitate during extrusion). Comparison between the 165/1 et 125/1 alloys lattice parameters [20] leads to a calculated Mo amount in solid solution lower than the aimed value. This is consistent with the reduction of the total Mo amount detected by the chemical analysis (Table II).

The alloys in the as-consolidated condition present noticeable differences in the lattice parameter. To determine why this is we have calculated the Fe/Mo ratio in the silicide by assuming the following hypotheses: there are no iron or silicon atoms in the matrix and are only considered the stoichiometric deviations of the silicide composition due to silicon substitution in the aluminum lattice or molybdenum in the iron lattice (in other words the ratio of number of sites of Al + Si (114) and the number of sites of Fe + Mo (24) remains constant). The (Al + Si)/(Fe + Mo) ratio used (4.75) is reasonable since values can be found in literature for ranges of 4.72 to 4.81 for Al-Fe-Mo-Si alloys [9]. Using these hypotheses, the Mo concentration in the solid solution can be deduced from the matrix's lattice parameter. The chemical composition of the silicide and consequently the Fe/Mo ratio are then determined by knowing the alloy composition. Skinner *et al.* [8] proposed that the silicide lattice parameter must increase with the molybdenum content (decrease with the Fe/Mo ratio). In the as-consolidated condition, the parameter does increase in this way from the 2010/1 alloy ([Fe]/[Mo] = 10.2), 165/1 ([Fe]/[Mo] = 6.7), 125/1 ([Fe]/[Mo] = 5.2) to 205/1 ([Fe]/[Mo] = 5.3). The evolution of the silicide through an optimal composition seems to occur as shown in Table V by depletion of Mo in alloys 205/1

TABLE V Comparison between the aimed and calculated [Fe]/[Mo] ratio (left side columns). Comparison between the measured and extrapolated mean lattice parameters from Skinner *et al.* [8] for the silicide

Alloy	Aimed Fe/Mo	Calculated Fe/Mo	Measured a (Å)	Skinner *et al.* [8] a (Å)
2015/1	15/1	14.1/1	12.580 ± 0.02[a]	12.600 ± 0.002
2010/1	10/1	10.2/1	12.597 ± 0.009	12.609 ± 0.002
205/1	5/1	5.3/1	12.651 ± 0.013	12.635 ± 0.002
165/1	5/1	6.7/1	12.617 ± 0.008	12.613 ± 0.002
125/1	5/1	5.2/1	12.641 ± 0.012	12.631 ± 0.002

[a]Composition 2015/1, value obtained in the powder.

and 125/1 (slight decrease of the parameter) and by enrichment in the 2010/1 alloy (slight increase of the parameter). However this observation is not completely confirmed by the corresponding variations in the matrix. The calculated values of the [Fe]/[Mo] ratio and the respective measurements of lattice parameters are presented in Table V for the different alloys. These are very close to the values of the parameters extrapolated from the experimental results of Skinner *et al*. [8] for similar [Fe]/[Mo] ratios. It might be said that the calculated [Fe]/[Mo] ratios are very close to the aimed values (second left side column).

4.2. Microstructures

4.2.1. Morphology and stability of the silicides

The microstructural diversity observed in the powders can also be observed in the consolidated material. Longitudinal sections show band structures produced by extrusion process. The boundaries between the prior particles are revealed by different sizes and volume fraction of precipitates [20]. The same comment could be made for transverse sections. It seems that neither the degassing nor the hot extrusion modify the coarse precipitate morphologies.

As said before, the differences in powder particles' size and morphology, produced by changes in the solidification rate and/or in chemical composition, help to identify the boundaries between the prior powder particles in the consolidated material (Figs 10–12). The grain size changes with the type and distribution of precipitates, but the mean size is of the order of 1 μm. Only the cells walls are broken by the intense plastic shearing during extrusion (Figs 10–12). The fragments of the cell walls are identified as the cubic silicide through selected area diffraction pattern (SADP) (Fig. 13).

The morphology of the phases presented in the Figs 14 and 15, has already been reported for some ternary alloys such as Al-Fe-V, Al-Mn-Si [21, 22] and some quaternary alloys such as Al-Fe-V-Si, Al-Fe-Mn-Si [23–26]. In the ternary systems, these precipitates are identified as an icosahedral phase whose thermal stability decreases with an increase in silicon content [24]

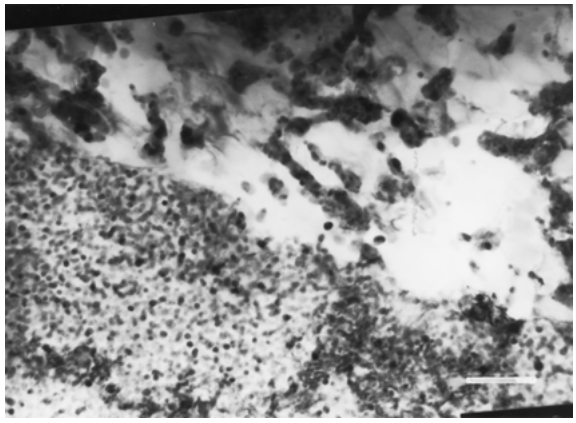

Figure 10 TEM observation of the boundary between two prior powder particles (marker = 0.6 μm, alloy 165/1): one side presents a fine precipitation of silicides and the other shows fragments of cells produced by the plastic shearing.

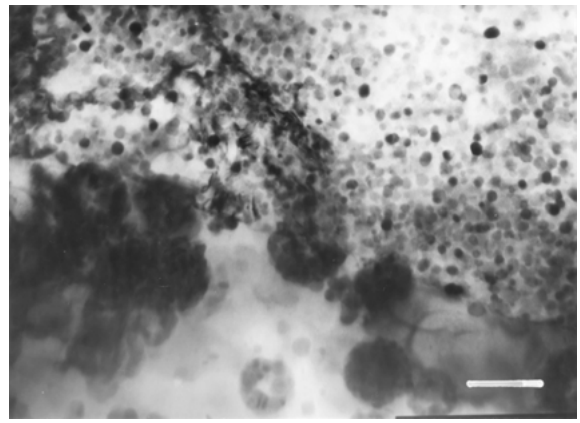

Figure 11 Other TEM observations of the boundary between two prior powder particles (marker = 0.5 μm, alloy 165/1): one particle exhibits a fine precipitation of silicides but conversely to Fig. 10 no shearing of the composite precipitates is detected.

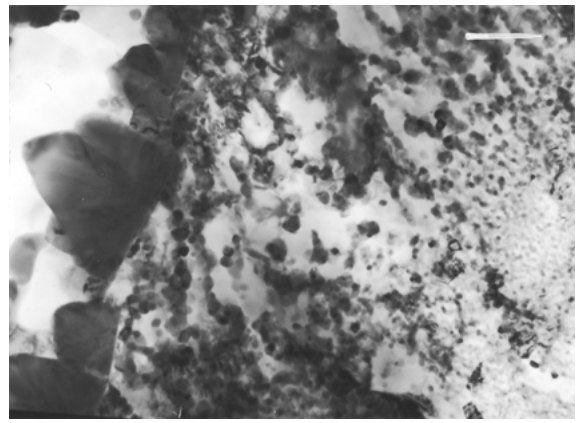

Figure 12 TEM observation of a gradual decrease of silicide size with the distance to the particle boundary (bottom left corner to the top right corner) due to changes in thermal regime (marker = 0.5 μm, alloy 205/1). In the adjacent particle, the microstructure changes from some coarse precipitates in the particle surface to a solid solution.

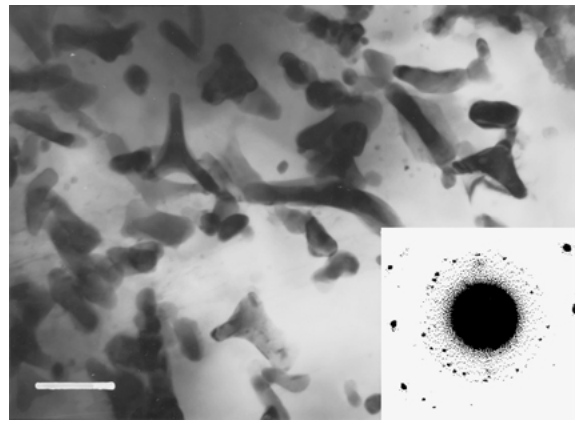

Figure 13 TEM observation of cell walls dispersed by the plastic deformation (marker = 0.3 μm, alloy 165/1). The silicide phase is identified by the size of the ring pattern of the SADP.

thus leading to cubic phase formation [22]. It is possible that, for the Al-Fe-Mo-Si alloys studied, the product of the transformation was observed because the precipitates consisted of several cubic phase grains, as shown in Fig. 15. Only one crystallite is under Bragg condition ($\langle 001 \rangle$cubic zone axis). This small crystal seems to grown from a central seed (see arrow).

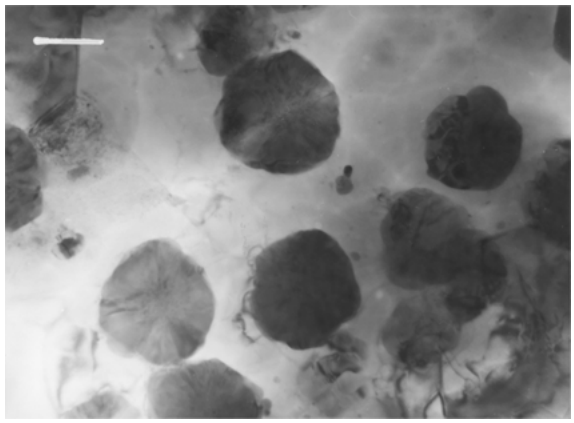

Figure 14 TEM observation of a dense precipitation of bulky silicides (marker = 0.6 μm, alloy 205/1).

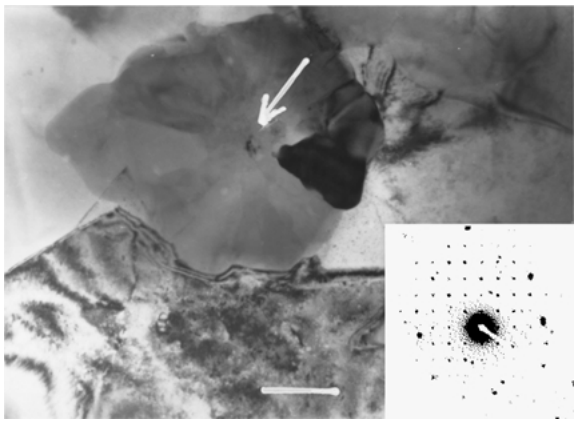

Figure 15 TEM observation of a precipitate (marker = 0.3 μm, alloy 205/1): the diffraction pattern obtained from the diffracting small grain (arrow) corresponds to the (100) silicide plane.

4.2.2. Possible silicide formation

The different morphologies of the silicides presented are related to the local variations of composition and/or solidification rate. According to the shape and/or nature of the inner core of the precipitate one can distinguish: (i) nodular precipitates which develop radially from a more or less visible seed; (ii) composite precipitates with an inner core which is a mixture of an α-matrix and a precipitated phase.

4.2.2.1. Nodular precipitates. The nodular precipitates with radial development showed Figs 14 and 15 are formed by several crystallites of cubic phase. When the selected area aperture completely covers the nodule, the diffraction patterns obtained have interesting symmetries (Fig. 16a and b). These are respectively very similar to the five and twofold symmetries observed in the icosahedral phases.

However, according to the spot chosen in the diffraction pattern (Fig. 16a) in order to obtain the dark field, different crystallites are placed in Bragg's condition (Fig. 16c and d) (this is in agreement with the observation of Fig. 15). This means that there is an orientation relationship between the crystallites. These ones seem to grow radially from a nucleation seed, which is sometimes visible (Fig. 15). Some orientation relationship should be maintained during the change from an original structure (that of the nucleus) to a body centered cubic (that of the silicides) that was probably induced by a reduction in the solidification rate.

In similar alloys, the seeds have been identified as quasicrystals [22 and 25]. The icosahedral phases are often represented as a three-dimensional aperiodic array of Penrose rhombohedra, but it is also possible to consider such phases as either the limit of a sequence of periodic structures with ever larger unit cells ("approximants") or as the disordered body-centered cubic structure with a motif formed by Mackay icosahedron [27]. For the Al-Mn-Si alloys [22], during the transformation from disordered to ordered bcc structure, the three edges of the cube are parallel to the three axes of twofold symmetry of the icosahedron. The four $\langle 111 \rangle$ directions of the cube are parallel to the quasicrystal threefold symmetry axes. Finally the fivefold symmetry axis is very close to the $\langle 530 \rangle$ cubic direction. When several crystallites have grown from a common seed, the continuity at the interface quasicrystal seed/cubic silicide leads to an orientation relationship such that the icosahedral units are parallel one crystallite to another. This could be expressed in terms of twinning around an irrational axis $[1\tau 0]$.

The formation of twinned structures does not necessarily require an icosahedral seed. Because of to the small size of the cores observed in these nodular precipitates, it was not possible to obtain a direct confirmation of their crystallographic structure. However, in rapid solidification, the cooling of the liquid is rapid enough to freeze the disordered icosahedral clusters already probably present in the liquid state [28]. The final size of the unstable quasicrystalline phase increases with the quenching rate of the powders. This final size must then range from atomic clusters [26] to micronic size precipitates. It is therefore possible to observe extreme examples where the solidification rate is either so high that the nodules are completely constituted by an icosahedral phase (confirmed by Benderski *et al.* [25] in the Al-Mn-Si alloys and by Skinner *et al.* [21] in the Al-Fe-V alloys) or where for lower solidification rate (this study) the cubic phase is mainly detected. This confirms that higher cooling rates are more readily achieved through melt spinning than through centrifugal atomization.

4.2.2.2. Composites precipitates. Other than "extreme" figures (pure icosahedron or pure body-centered cubic), it is also possible to observe intermediate morphologies. Mandal *et al.* [26], for instance, found diffraction patterns where there was an overlap of silicide rings and fivefold symmetry pattern from the icosahedral phase. In the same way, aggregates observed in Al-Fe-Mo-Si alloys (Fig. 17a) formed by coarse crystallites around a coarse core gave rise to a threefold symmetry diffraction pattern (Fig. 17b) with, near the transmitted spot, a (111) pattern of the bcc phase. The core will still diffract whatever the chosen spot, and this will happen for the three axes of symmetry (black field images 17c and d, are obtained respectively from the two marked spots from the diffraction patterns 17b). As suggested by Koskenmaki *et al.* [22] and Benderski *et al.* [25], the central grain is probably a quasicrystal

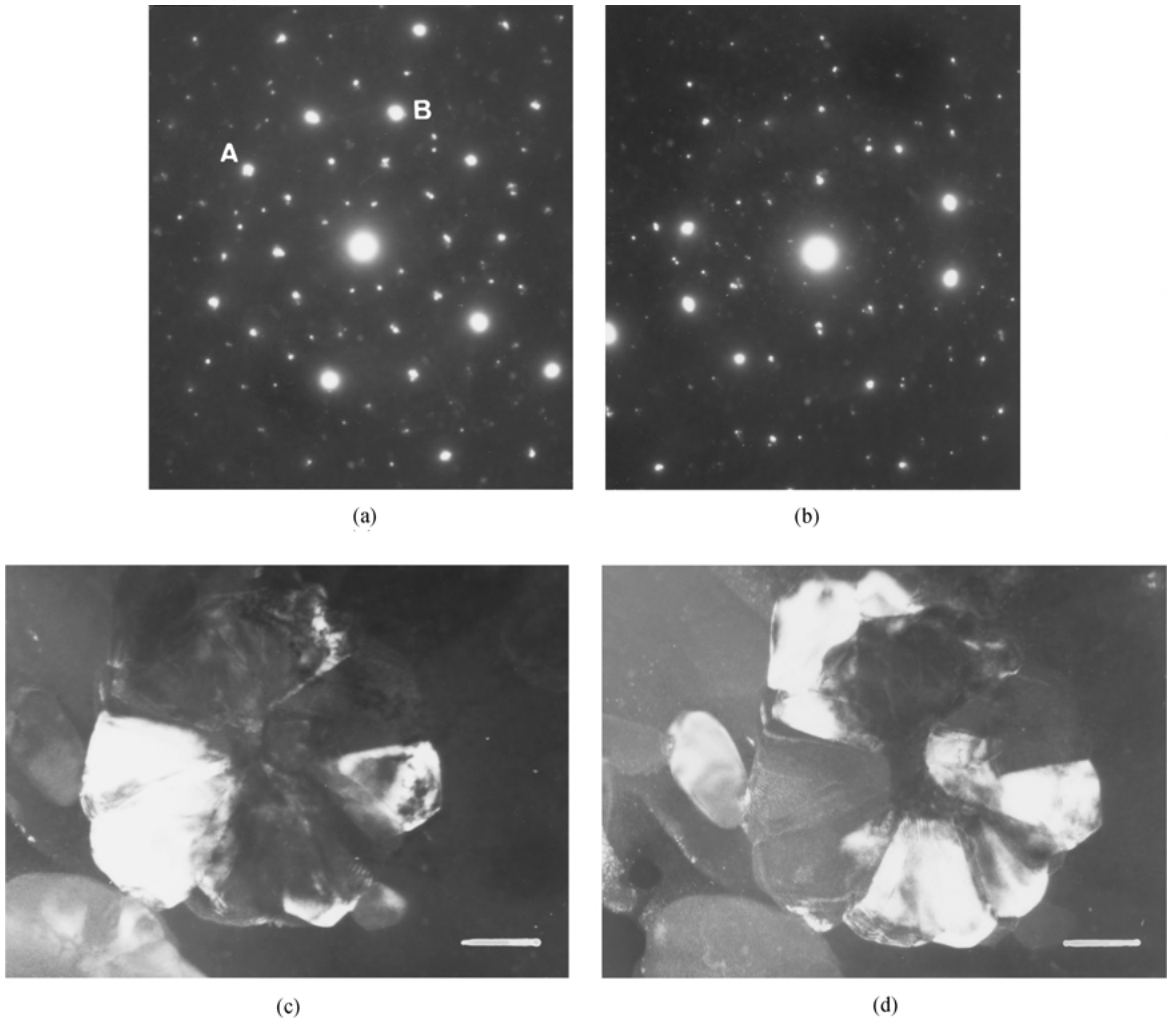

Figure 16 When the selected area aperture is larger than the precipitate (micrographs 16c and 16d), the diffraction patterns show symmetries close to the observed ones in the icosahedral phases (five fold symmetry for 16a and two fold for 16b). Dark field images obtained by selection of two spots A and B of the diffraction pattern 16a proving that each spot is produced by a different crystallite (marker = 0.25 μm, alloy 205/1).

or a mixture of icosahedral and cubic phases, the outer crystallites could be put out of Bragg's condition.

Since there is no reason for the icosahedral and body center cubic phases to have the same composition, we could think, as did Koskenmaki *et al.* [22], that the quasicrystal would reject the excess of silicon and aluminum during its growth, this stabilizing the bcc phase which will precipitate in a coherent way around the quasicrystalline core. A second hypothesis can be found in literature: during solidification, the quasicrystalline phase is formed and grown in a liquid which solidifies as the α-Al matrix. In subsequent cooling, the interdiffusion allows for the transformation of the periphery of the quasicristal to an aggregate of crystallites having a twinning relationship among them. The interface depletion thus leads to the formation of an inner layer of aluminum [29]. In the micrograph 17d, this inner layer of aluminum is clearly visible. The rotations made to pass from the $[\bar{1}\tau 0]$ plane (fivefold symmetry) to the $[\bar{\tau}^2 10]$ plane (threefold symmetry) and finally to the $[\bar{1}00]$ plane (twofold symmetry), accurately match the theoretical values proposed by Chattopadhyay *et al.* [30].

Other types of composites have been detected in these Al-Fe-Mo-Si alloys. For instance, the silicide crystallites of the aggregate presented in Fig. 9, did not present any preferential orientation because the diffraction rings did not show any particular reinforcement. Because the composites' diameter was larger than the foil thickness, the general aspect could be very variable according to the surfaces position in comparison with the precipitate center. It is made up of a shell of fine silicide crystallites surrounding a core which is essentially Al matrix (confirmed by SADP). Benderski *et al.* [25] have observed the same type of morphology in Al-Fe-Mn-Si alloys. The origin of the formation of such composites is not clear. Mandal *et al.* [26] proposed that an amorphous phase nucleates and then decomposes, rejecting alloy elements at the periphery thus producing an aluminum core surrounded by silicides. The same authors suggest that this amorphous phase would be a precursor of the quasicrystalline phase. In order to be in agreement with Maret *et al.* [28]'s calculations, it would be necessary for a icosahedral short-range order packed by some atomic clusters of the amorphous phase to exist. Indeed, it has been recently found [31], that the short-range atomic configuration in the amorphous phase of Al-Fe-Ce alloys is very similar to that in the quasicrystalline phase.

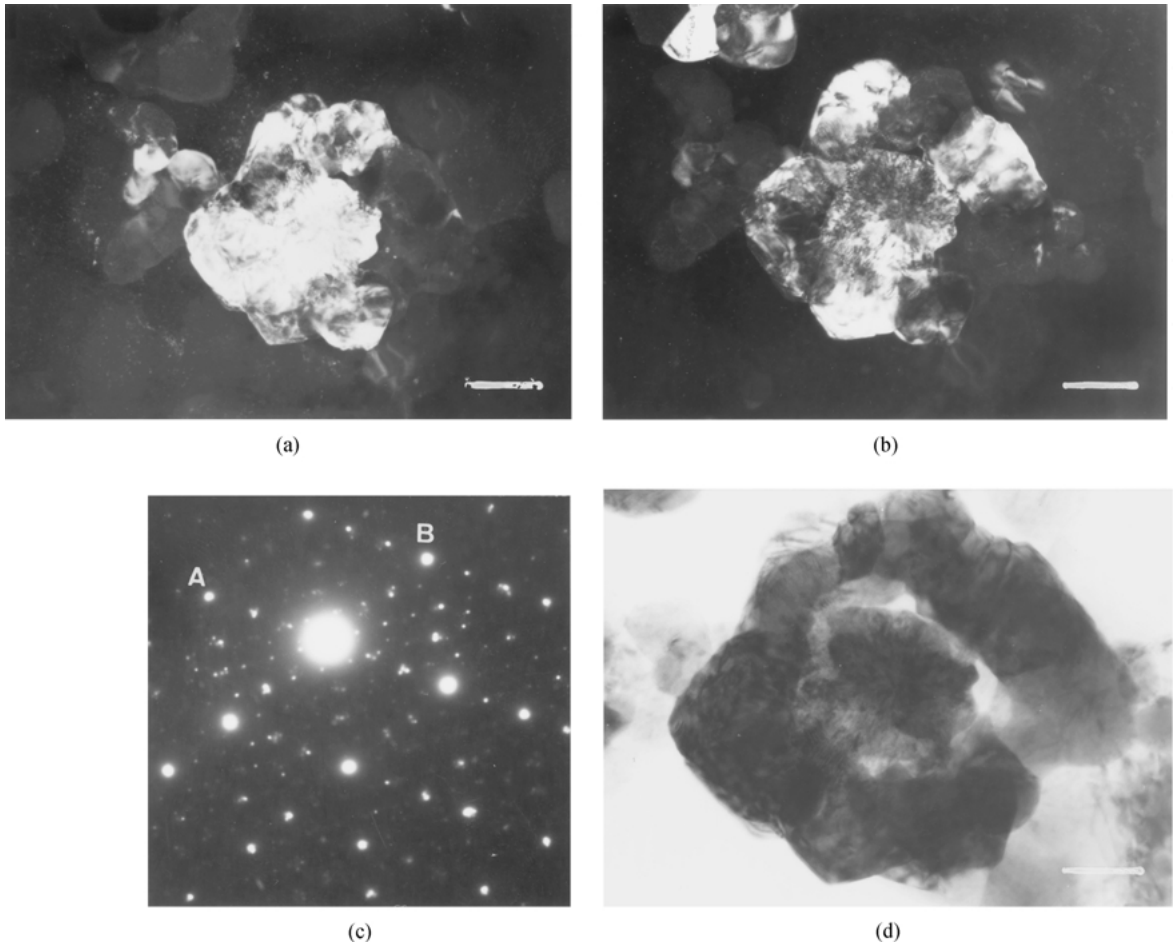

Figure 17 Observation of a silicides aggregate (17a) and corresponding (111) threefold symmetry diffraction pattern (17b). The dark field images (17c and d) are obtained from the two marked spots (A and B) of 17b (marker = 0.25 μm, alloy 125/1). It is possible to note the diffraction pattern from the (111) plane (bcc). In the bright field micrograph (17a), an inner layer of aluminum can be noticed (marker = 0.17 μm).

5. Conclusions

Quaternary Al-Fe-Mo-Si alloys have been produced through the rapid solidification route. A high yield stress is expected from a fine dispersion of intermetallic phases while a high thermal stability should result from a low solubility and diffusivity of the transition elements. The size of the dispersoids ranges between 50 nanometers and 0.8 micrometers with a mean value larger than that noticed on AlFeVSi alloys produced through planar flow casting. This weakness could be overcome by improving the rapid solidification process. These alloys exhibit strong microstructural inhomogeneities which highlight not only changes in thermal history within a particle but also differences from particle to particle. The freezing conditions depend on prior undercooling which is very much influenced by nucleation event. The absence of contact with a mould wall and the small size of the particle will limit the number of potential nuclei. Hence, the nucleation event is too random to be controlled unless undercooling is high enough to prevent phase precipitation.

The α-matrix and the cubic $Al_{13}(FeMo)_3Si$ are detected by XRD in the as atomized condition or after extrusion, the equilibrium $Al_{12}Mo$ phase in two alloys after heat treatment. The silicide can exhibit different morphologies. Its thermal stability is confirmed by the absence of the $Al_{13}Fe_4$ equilibrium phase. One important conclusion from TEM observations is the link between five-fold symmetry SADPs and twinned polycrystalline aggregates of cubic silicides. Such a twinning is initiated on a seed and imposed by the orientation relationship between the seed and the silicide. This nucleus will have either an amorphous or, most probably, a icosahedral structure.

This study has shown that, due to the good thermal stability of the silicide, high temperature associated with an extrusion process is compatible with the rapid solidification route used here. The next steps will be firstly, to link the microstructure to the mechanical properties of the consolidated material and secondly, to quantify the influence of molybdenum on the thermal stability of the silicide and on the ductility drop during forming.

References

1. L. ANGERS, Y. CHEN, M. E. FINE, J. R. WEERTMAN and M. S. ZEDALIS, in "Aluminum Alloys, Physical and Mechanical Properties," edited by E. A. Starke and T. H. Sanders Jr. (EMAS, 1986) p. 321.
2. D. J. SKINNER, R. L. BYE, D. RAYBOULD and A. M. BROWN, *Scripta Met.* **20** (1986) 867.
3. D. J. SKINNER, in "Dispersion Strengthened Aluminum Alloys," edited by Y.-W. Kim and W. M. Griffith (TMS, 1988) p. 181.
4. J. C. LEE, S. LEE, D. Y. LEE and N. J. KIM, *Met. Trans.* A **22A** (1991) 853.

5. S. LEE, D. Y. LEE and N. J. KIM, *Mater. Sci. Eng.* A **147** (1991) 33.
6. D. J. SKINNER, M. S. ZEDALIS and P. GILMAN, *ibid.* A **119** (1989) 81.
7. E. BOUCHAUD, L. KUBIN and H. OCTOR, *Met. Trans.* A **22A** (1991) 1021.
8. D. J. SKINNER, R. L. BYE, D. RAYBOULD, A. M. BROWN and M. S. ZEDALIS, in "Processing of Structural Metals by Rapid Solidification," edited by F. H. Froes and S. J. Savage (ASM International, Orlando, 1986) p. 291.
9. V. K. VASUDEVAN and H. L. FRASER, *Scripta Met.* **21** (1987) 1105.
10. A. ZIANI and G. MICHOT, *Inter. Jal of Non Equilibrium Processing* **9** (1996) 305.
11. N. I. VARICH, L. M. BUROV, K. YE. KOLESNICHENKO and A. P. MAKSIMENKO, *Phys. Met. Metallogr.* **15** (1963) 111.
12. A. F. POLESYA and A. I. STEPINA, *ibid.* **30** (1970) 35.
13. C. G. LEVI and R. MEHRABIAN, *Met. Trans.* A **13A** (1982) 221.
14. W. J. BOETTINGER and J. H. PEREPEZKO, in "Rapidly Solidified Crystalline Alloys," edited by S. K. Das, B. H. Kear and C. M. Adam (TMS-AIME, Warrendale, PA, 1985) p. 21.
15. H. BILONI and B. CHALMERS, *Trans. TMS-AIME* **233** (1965) 373.
16. Y. WANG, G. W. LORIMER and F. R. SALE, *Scripta Met.* **31** (1994) 1337.
17. H. OCTOR, E. BOUCHAUD, F. ZOZIME and M. MARTY, Technical Report no 6/3683 M (ONERA, 1991) p. 9, 37.
18. H. OCTOR, E. BOUCHAUD and M. MARTY, Technical Report no 8/3683 M (ONERA, 1992), p. 10, 13, 33.
19. W. J. BOETTINGER and J. H. PEREPEZKO, in "Rapidly Solidified Alloys," edited by H. H. Libermann (Marcel Dekker, New York, 1993) p. 68.
20. M. C. S. DE MACÊDO, PhD thesis, INPL, France, 1995.
21. D. J. SKINNER, V. R. V. RAMANAN, M. S. ZEDALIS and N. J. KIM, *Mater. Sci. Eng.* **99** (1988) 407.
22. C. KOSKENMAKI, H. S. CHEN and K. V. RAO, *Phys. Rev.* B **33** (1986) 5328.
23. N. J. KIM, *Int. J. Rap. Solid* **6** (1991) 175.
24. V. R. V. RAMANAN, D. J. SKINNER and M. S. ZEDALIS, *Mater. Sci. Eng.* A **134** (1991) 912.
25. L. A. BENDERSKY, J. W. CAHN and D. GRATIAS, *Phil. Mag.* B **60** (1989) 837.
26. R. K. MANDAL, G. V. S. SASTRY, S. LELE and S. RANGANATHAN, *Scripta Met.* **25** (1991) 1477.
27. V. ELSER and C. L. HENLEY, *Phys. Rev. Lett.* **55** (1985) 2883.
28. M. MARET, F. LANÇON and L. BILLARD, *J. Phys. Condens. Matter.* **6** (1994) 5791.
29. A. K. SRIVASTAVA and S. RANGANATHAN, *Scripta Met.* **27** (1992) 1241.
30. K. CHATTOPADHYAY, S. LELE, R. PRASAD, S. RANGANATHAN, G. N. SUBBANNA and N. THANGARAJ, *ibid.* **19** (1985) 1331.
31. C. ZHANG, Y. WU, X. CAI, F. ZHAO, S. ZHENG, G. ZHOU and S. WU, *Mater. Sci. Eng.* A **323** (2002) 226.

Received 9 January 2001
and accepted 24 December 2002